

# SOI-MEMS Bulk Piezoresistive Displacement Sensor: A Comparative Study of Readout Circuits

Mohammad Maroufi<sup>ID</sup>, Nastaran Nikooienejad<sup>ID</sup>, Mohammad Mahdavi<sup>ID</sup>,  
and S. O. Reza Moheimani<sup>ID</sup>, *Fellow, IEEE*

**Abstract**—Performance of several readout circuits, when applied to a MEMS-based bulk piezoresistive displacement sensor is compared in this study. The sensor comprises a pair of tilted clamped-guided silicon beams whose bulk piezoresistivity is used for displacement sensing. Wheatstone half-bridge, constant-voltage, and constant-current circuits are implemented to measure resistance changes of this sensor. We report full characterization of the sensor with these circuits and explore the sensor's important characteristics such as linearity, bandwidth, and noise. The results reveal that the constant-current circuit provides the highest sensitivity at equal-power bias condition. We find that the resolution of the sensor is degraded from 1.6 nm with the Wheatstone half-bridge and constant-voltage circuits to about 4.2 nm with the constant-current configuration. In the frequency domain, the sensor captures the full dynamics of the MEMS nanopositioner up to 20 kHz with all readout circuits. [2019-0168]

**Index Terms**—Piezoresistive displacement sensor, tilted clamped-guided beam, microelectromechanical system (MEMS) nanopositioner, constant-current circuit, constant-voltage circuit, Wheatstone bridge.

## I. INTRODUCTION

**D**ISPLACEMENT measurement is needed in numerous microelectromechanical system (MEMS)-based devices. Inertial sensors, microgrippers, microcantilevers, and MEMS positioners are examples of such devices that depend on accurate displacement measurements. It is highly desirable and in many cases a requirement that displacement sensors are integrated into the MEMS device. To address this need, various measurement methods have been proposed in the literature with capacitive [1], electrothermal [2], [3], piezoelectric [4], and piezoresistive sensing mechanisms [5], [6] being the primary choices.

These mechanisms have been successfully miniaturized for on-chip applications. However, to realize each displacement sensing concept successfully, the designer needs to make a number of technical trade-offs, e.g. see the reviews [7], [8].

Manuscript received July 21, 2019; revised September 21, 2019; accepted October 26, 2019. Subject Editor D.-I. D. Cho. (*Corresponding author: S. O. Reza Moheimani.*)

The authors are with the Erik Jonsson School of Engineering and Computer Science, The University of Texas at Dallas, Richardson, TX 75080 USA (e-mail: mohammad.maroufi@utdallas.edu; nastaran.nikooienejad@utdallas.edu; mmahdavi@utdallas.edu; reza.moheimani@utdallas.edu).

Color versions of one or more of the figures in this article are available online at <http://ieeexplore.ieee.org>.

Digital Object Identifier 10.1109/JMEMS.2019.2952547

In this work, we concentrate on piezoresistive displacement sensors. These sensors can measure displacement from DC to higher frequencies. Their ability to measure static deflections makes them superior to piezoelectric sensors, and their high-bandwidth and low-drift sensing properties compare positively with electrothermal sensors [9]. In the case that the chip space is limited, the piezoresistor sensors can be a better proposition than capacitive sensors due to their small footprint. Finally, implementation of readout circuitry for piezoresistive sensors may be a less complex exercise compared to their capacitive counterparts [7], [8].

Piezoresistive displacement sensors are typically implemented by producing highly-doped regions on the device flexures. This procedure, however, requires additional mask and microfabrication steps which may increase the fabrication cost and is not always available through standard commercial microfabrication processes. To address this issue, we previously proposed a displacement sensing mechanism that utilizes bulk piezoresistivity of silicon [10], [11]. This sensor achieves a nanometer-range resolution, and comprises two pairs of slightly tilted silicon beams. The top surface of these beams is doped, allowing their bulk piezoresistivity to be used for displacement sensing. This eliminates the need for extra masking procedure to realize highly-doped regions. We reported successful implementation of this method in a MEMS nanopositioner in [12] and a MEMS force sensor in [13].

The sensor can be electrically modeled as two variable resistors tied up together at one end with the other ends floating. In [12], [13], we used a Wheatstone half-bridge as a readout circuit to convert the resistance changes in the bulk piezoresistive sensor to a voltage output. Wheatstone bridge is widely used in MEMS devices to convert small resistance changes to voltage output e.g. see [14]–[19]. This circuit can be driven either with voltage or current [20], with the current-driven Wheatstone bridge being able to deliver a higher sensitivity [15]. It is well-understood that using Wheatstone bridge in a half-bridge configuration could lead to nonlinear behavior [7]. Moreover, the lumped resistors used in non full-bridge configurations may limit the sensitivity. For resolution enhancement, modulation-demodulation techniques and lock-in amplifications have been used [21], [22]. These techniques, however, limit the ultimate bandwidth of the sensor.

As an alternative to Wheatstone bridge, a transimpedance amplifier can be used to measure resistance variations.

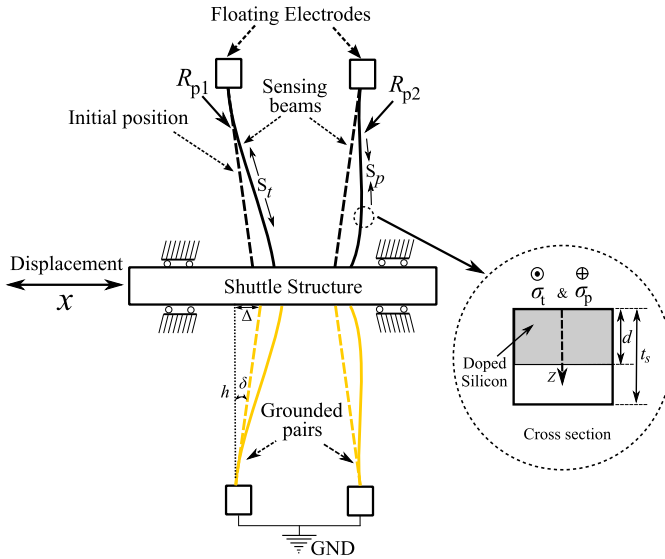


Fig. 1. The schematic of the piezoresistive displacement sensor. The shuttle structure moves rectilinearly. The cross section of the beam is presented in the close-up view, while the doping depth is schematically shown by the gray area. The mechanical stress along the beam (orthogonal to the cross section) can be tensile ( $\sigma_t$ ) and compressive ( $\sigma_p$ ) during the operation.

This circuit functions based on converting the current flowing in the sensing resistor to a voltage output. In contrast to the Wheatstone bridge, the voltage across the sensing element is constant, resulting in a more linear behavior. This circuit was used in [23] to measure piezoresistance of displacement sensor microfabricated in a piezoelectrically-actuated torsional microstage. Performance of transimpedance and Wheatstone bridge circuits were compared in [24] for electrothermal sensors in a MEMS nanopositioner. Higher sensitivity and repeatability were achieved with the transimpedance circuit.

In this paper, we investigate the performance of three readout circuits, namely Wheatstone bridge, constant-voltage (transimpedance), and constant-current circuits, when applied to our proposed bulk-piezoresistive displacement sensor. We derive analytical and system-level models for these configurations and perform detailed characterization of a bulk-piezoresistive sensor that we reported in [12].

The remainder of the paper continues as follows. In the next section, structure of the bulk piezoresistive sensor is detailed. The MEMS nanopositioner is introduced in Sec. III, and Sec. IV presents analytical modeling of the sensor. The readout circuits are further investigated in Sec. V. In Sec. VI, system-theoretic models of the sensor with constant-voltage and constant-current circuits are presented. Sec. VII details the experimental setup. The properties of the sensor with different readouts are compared in Sec. VIII, and Sec. IX concludes the paper.

## II. PIEZORESISTIVE SENSOR

Fig. 1 shows the schematics of the bulk piezoresistive sensor. The sensor features two pairs of slanted clamped-guided beams located on either sides of a shuttle structure. This structure exhibits mainly a rectilinear displacement with negligible rotation and/or displacement along other orthogonal directions. The sensor is fabricated as a part of a MEMS

nanopositioner using MEMSCap's SOIMUMPs process [25]. This silicon-on-insulator (SOI)-based process starts with a n-doped wafer with a 25  $\mu\text{m}$ -thick device layer. The bulk resistivity of the device layer is 1  $\Omega\cdot\text{cm}$  to 10  $\Omega\cdot\text{cm}$ . Initially, the n-type doping at the top surface of this layer is enhanced using a thermal diffusion technique to achieve a lower resistivity. This step leads to a sheet resistivity of 15 to 25  $\Omega/\text{sq}$  and increases the silicon piezoresistivity at the top surface of the device layer. The process is then continued by deposition and patterning of a gold layer as the metal conducting layer. The device layer is then patterned using deep reactive ion etch (DRIE) method, and finally using back-side substrate etch, the moving parts of the device are released. More details about the process can be found in [25].

As shown in Fig. 1, the top side pair of beams function as a sensor. A gold layer is deposited on the silicon beams in the other pair and they are electrically grounded. The beams feature a vertical length ( $h$ ) of 1 mm and are slightly tilted from their vertical position with respect to the shuttle structure, with the tilting angle being  $\delta=0.86^\circ$ . Due to the V-shaped configuration of the beams, as the shuttle structure undergoes a displacement in one direction, one sensing beam experiences a compressive axial force ( $S_p$  in Fig. 1), while the other endures a tensile load ( $S_t$ ). This longitudinal forces induce opposite resistance changes in the sensing beams due to their bulk piezoresistivity. While the sensing beams are jointly grounded at one end, the other electrically-floating ends are fed to a readout circuit to convert their resistance change to an output voltage. Note that the silicon beams in the second pair are gold-covered (shown in yellow color in Fig. 1), and thus their resistance change due to the silicon piezoresistivity is bypassed by the negligible resistance of the gold layer.

## III. MEMS NANOPositionER

In the work we reported in [12], the bulk piezoresistive displacement sensor is incorporated within a 2 degree-of-freedom (2DoF) MEMS nanopositioner. A scanning electron microscope (SEM) micrograph of the device is shown in Fig. 2. Electrostatic comb-drive actuators are implemented on four sides to provide the necessary force for the scan table to move bidirectionally along the X and Y axes. One shuttle beam on each side transfers the actuation force to the scan table via tethering beams shown in the close-up view. The bulk piezoresistive sensor is incorporated to measure the displacement of the shuttle structures on each side. The beams within the sensor also function as a component of the nanopositioner's mechanical suspension system. While the design and characterization of this MEMS nanopositioner is detailed in [12], in this work, we employ the device as a platform to explore performance of its displacement sensor with different readout circuits. Experiments are performed on one of the piezoresistive displacement sensors shown in the close-up view in Fig. 2. Due to the symmetry, similar results are expected for the remaining sensors.

## IV. ANALYTICAL MODEL OF THE SENSOR

The sensing beams can be modeled as two varying resistors which are electrically grounded at their common end. Prior to

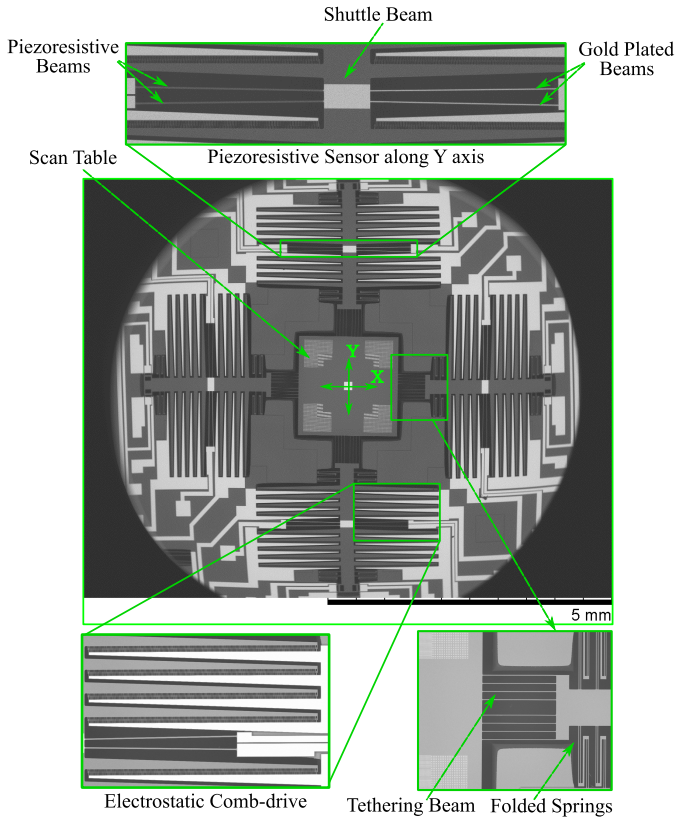


Fig. 2. The SEM micrograph of the 2DoF MEMS nanopositioner. The scan table at the center has the dimension of  $1.8\text{ mm} \times 1.8\text{ mm}$ . Bulk piezoresistive sensors are implemented on all sides of the device to measure the displacement of the shuttle beams. The close up view on the top shows one of the sensors along Y axis. Electrostatic actuators and a part of the flexural mechanism for the shuttle beam are also shown in the close up views.

exploring the readout circuits, we present a model of the piezoresistive sensor, which relates the displacement of the shuttle structure to the resistance changes in the sensing beams.

In Fig. 1, the shuttle displacement induces a tensile longitudinal force ( $S_t$ ) in one sensing beam and a compressive axial force ( $S_p$ ) along the other. We may write [11]:

$$(|S_t| + |S_p|) = K_c x. \quad (1)$$

where  $K_c$  is a function of the geometrical properties of the sensing beams, including their length and inclination angle, and  $x$  is the input displacement. Denoting the cross section area of the beams by  $A_c$  and using the definition of normal stress, for (1) we have:

$$\sigma_{tp} = \frac{K_c x}{A_c} \quad (2)$$

where

$$\sigma_{tp} = (|\sigma_t| + |\sigma_p|) \quad (3)$$

Here,  $\sigma_t$  and  $\sigma_p$  are the normal tensile and compressive stresses. In the Appendix, we show that resistance change of the sensing beam under tension can be stated as:

$$R_t \cong R_0 (1 - |\sigma_t| \pi_0 K') \quad (4)$$

where  $K'$  is a function of the beams cross section dimensions as well as doping profile. Similarly, for the compressive load we have:

$$R_p \cong R_0 (1 + |\sigma_p| \pi_0 K'). \quad (5)$$

From (4) and (5), we conclude that resistances of the two beams undergo opposite variations for the same displacement. This enables the possibility of differential sensing.

## V. READOUT CIRCUITS

We investigate three readout configurations, namely Wheatstone half-bridge, constant-voltage (C.V.) and constant-current (C.C.) circuits to translate the opposite resistance changes in the sensing beams to an output voltage. The schematic of these circuits are shown in Fig. 3 and their outputs are analytically explored in this section.

### A. Wheatstone Half-Bridge

Due to its simple structure, a Wheatstone half-bridge can be the primary option for mapping differential resistance changes to an output voltage. Shown in Fig. 3a, the voltages  $V_p$  and  $V_q$  on the sensing beams are obtained as:

$$V_{p,q} = \frac{V_b R_{t,p}}{R_t + R_p} \quad (6)$$

On the second stage of this circuit,  $V_p$  and  $V_q$  are differentially amplified with the gain of  $A$ , resulting in the following output voltage:

$$V_{out} = A (V_p - V_q). \quad (7)$$

Replacing  $R_t$  and  $R_p$  from (4) and (5) in (7), we obtain the output voltage of the bridge ( $V_{ow}$ ) as:

$$V_{ow} = \frac{-AV_b K' \pi_0 R R_0}{(R + R_0)^2} \times \left[ \frac{\sigma_{tp}}{(R + R_0[1 - \sigma_t \pi_0 K'])(R + R_0[1 + \sigma_p \pi_0 K'])} \right] \quad (8)$$

Considering (2),  $\sigma_{tp}$  and the shuttle structure displacement ( $x$ ) are linearly dependent. Therefore,  $V_{ow}$  is not a linear function of  $\sigma_{tp}$ , and thus  $x$ . However, assuming  $(\sigma_t \pi_0 K') \& (\sigma_p \pi_0 K') \ll 1$  and replacing  $\sigma_{tp}$  from (3), the voltage output can be approximated as follows:

$$V_{ow} \cong -AV_b \pi_0 K' K_c \frac{R R_0}{A_c (R + R_0)^2} x. \quad (9)$$

Knowing the sensor output, its gain can be defined as the ratio of the output voltage to the input displacement (i.e.  $|V_{out}/x|$ ). Using (9), the gain for the Wheatstone half-bridge is found to be:

$$g_w = AV_b \pi_0 K' K_c \frac{R R_0}{A_c (R + R_0)^2}. \quad (10)$$

### B. Constant-Voltage Circuit

The constant-voltage readout circuit is shown in Fig. 3b. The operational amplifiers (op-amps) maintain the sensing beams'

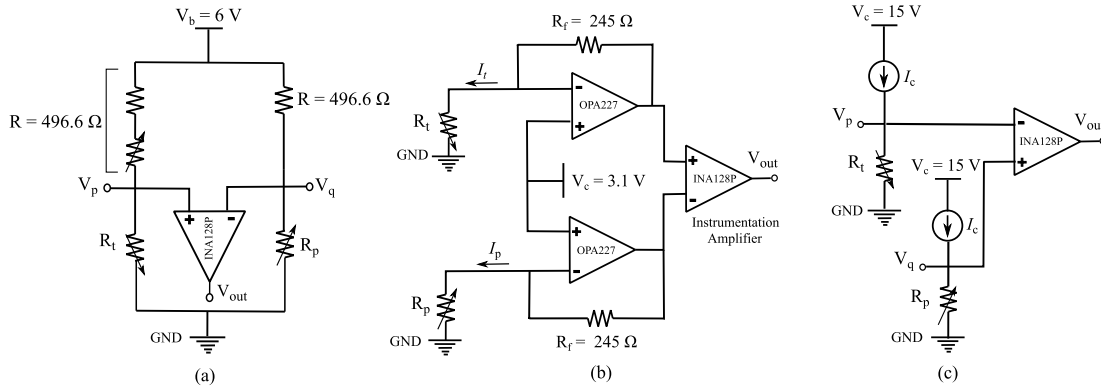


Fig. 3. Three readout circuits for mapping resistance changes in the piezoresistive sensing beams to an output voltage. (a) Wheatstone half-bridge, (b) constant-voltage drive, and (c) constant-current drive. At zero displacement input, the voltage at the output of each circuit is nullified using a potentiometer.

voltages at  $V_c$  throughout the sensor operation; in contrast to the Wheatstone half-bridge where this voltage is variable. In constant-voltage circuit, the output voltage is a function of the current flowing through the sensing beams ( $I_t$  and  $I_p$ ) and the gain of the differential amplifier  $A$ , obtained as:

$$V_{ov} = AR_f (I_t - I_p). \quad (11)$$

Using (2), and the expressions derived for  $I_t$  and  $I_p$  in the Appendix, we find  $V_{ov}$  as a function of  $x$  as follows:

$$V_{ov} = AR_f \frac{V_c}{A_c R_0} \pi_0 K' K_c x. \quad (12)$$

The sensor gain with the constant-voltage readout circuit can then be obtained from (12) as:

$$g_v = AR_f \frac{V_c}{A_c R_0} \pi_0 K' K_c. \quad (13)$$

This relation indicates that the output voltage is a linear function of the input displacement.

### C. Constant-Current Circuit

The C.C. readout circuit is shown in Fig. 3c. Here, two current sources are employed to maintain a constant bias current ( $I_c$ ) through the sensing beams. The second stage differentially amplifies the voltage generated on the beams (i.e.  $V_p$  and  $V_q$ ). The output voltage thus can be expressed as:

$$V_{oc} = A (V_q - V_p) = A I_c (R_p - R_t). \quad (14)$$

By replacing the resistance obtained in (4) and (5) in (14),  $V_{oc}$  can be described as a linear function of displacement, similar to the C.V. circuit. That is:

$$V_{oc} = \frac{A I_c \pi_0 R_0 K' K_c}{A_c} x \quad (15)$$

From (15), the sensor gain with C.C. circuit ( $g_c$ ) is obtained as:

$$g_c = \frac{A I_c \pi_0 R_0 K' K_c}{A_c}. \quad (16)$$

The sensor gain is a function of the sensor's geometry and material properties as well as the bias current.

## VI. SYSTEM-THEORETIC MODEL

So far, the output voltage of the readout circuits are obtained as a function of the input displacement, and we showed

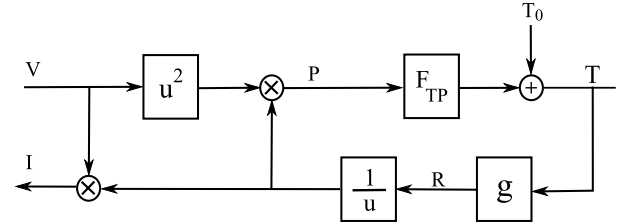


Fig. 4. A system-level model for one of the sensing beams.

that the sensor with constant-voltage and -current circuit is expected to function linearly. During the sensor operation, however, the sensing beams temperature can change due to the Joule heating, which perturbs their electrical resistance and consequently the sensor output. Including this effect in models derived in Sec. (IV), however, can make the modeling complicated without providing further insight into the sensor behavior. In order to include the thermal effect, we use a system-theoretic method, reported in [26], [27]. Here, the focus is only on the constant-voltage and -current circuits due to their linearity.

Fig. 4 presents a system-level model for one of the sensing beams, where two operators are assumed. Here,  $F_{TP}$  maps the electrical power delivered to the beam to its temperature, while  $g(\cdot)$  relates the beam's temperature ( $T$ ) to its electrical resistance ( $R$ ). A first or third order transfer function can be considered for  $F_{TP}$  as shown in [26] for silicon heaters. The operator  $g(\cdot)$ , can be realized as a memory-less polynomial function or a look-up table as discussed for silicon heaters in [26] and for a silicon electrothermal actuator in [28].

The nonlinear model in Fig. 4 can be linearized assuming small resistance variations. Fig. 5 shows linearized models of both configurations when perturbed by an input mechanical stress. Although we only consider the compressive input stress ( $\tilde{\sigma}_p$ ), the model is equally applicable to the tensile stress. The perturbation in the power ( $\tilde{P}$ ) and the temperature ( $\tilde{T}$ ) in the presence of an input stress is found to be:

$$\tilde{P} = \frac{2V_0}{R_0} \tilde{V} - I_0^2 \tilde{R} \quad (17a)$$

$$\tilde{T} = F_{T_0} \tilde{P}. \quad (17b)$$



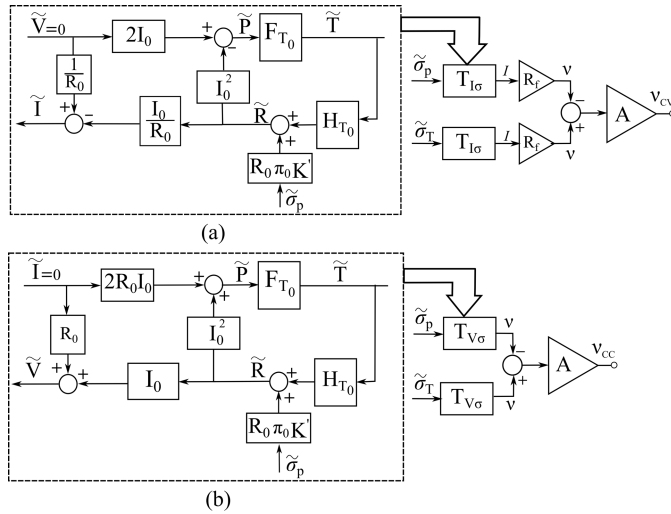


Fig. 5. The system-theoretic model of a sensing beam implemented within (a) constant-voltage and (b) constant-current readout circuits.

We derived the electrical resistance of the sensing beams in (5). Considering the temperature-dependency of the initial resistance ( $R_0$ ) and silicon piezoresistive coefficient ( $\pi$ ), we can obtain the resistance perturbation  $\tilde{R}_p$  as:

$$\tilde{R}_p = g'_T \tilde{T} \left( 1 + \pi_0 \sigma_{P_0} K' + R_0 K' \sigma_{P_0} w_0 \tilde{T} \right) + R_0 K' \tilde{\sigma}_p \pi_0 \quad (18)$$

where  $g' = \frac{\partial R_0}{\partial T} |_{T_0}$  and  $w_0 = \frac{\partial \pi}{\partial T} |_{T_0}$ . The first two terms in (18) capture the variation in the beam resistance due to a temperature change, while the third term is a consequence of the input mechanical stress. The resistance perturbation in (18) can be re-written as:

$$\tilde{R}_p = H_{T_0} \tilde{T} + R_0 \tilde{\sigma}_p \pi_0 k \quad (19)$$

where

$$H(T_0) = g'_T (1 + \pi_0 \sigma_{P_0} K') + R_0 \sigma_{P_0} w_0 K'. \quad (20)$$

To find a relationship between the perturbation in the resistance, current, and voltage, we may use the Ohm's law as applied to the sensing beam, i.e.:

$$\tilde{V} = \tilde{R} I_0 + R_0 \tilde{I}. \quad (21)$$

The model in Fig. 5a represents the constant-voltage circuit, which is obtained knowing the fact that the perturbation of the voltage on the sensing beams is zero. The transfer function from the input stress to the perturbation in the current flow through the sensing beam ( $T_{I\sigma}$ ) is:

$$T_{I\sigma} = \frac{-I_0 \pi_0 K'}{1 + I_0^2 H_{T_0} F_{T_0}}. \quad (22)$$

From the input mechanical stress to the temperature change of the beam ( $T_{T\sigma}$ ) the following transfer function can also be obtained.

$$T_{T\sigma} = \frac{-R_0 \pi_0 K' I_0^2 F_{T_0}}{1 + I_0^2 H_{T_0} F_{T_0}} \quad (23)$$

Designating the gain of amplifier in Fig. 5a by  $A$  and using (22), the output voltage is found as:

$$V_{CVo} = A I_0 R_f \frac{\pi_0 K'}{1 + I_0^2 H_{T_0} F_{T_0}} \sigma_{ip}. \quad (24)$$

From (24), we observe that the constant-voltage circuit maintains its linear behavior in the presence of beam's thermal effects at small mechanical stress levels. In addition, the transfer functions  $T_{I\sigma}$  and  $T_{T\sigma}$  resemble a system with a negative feedback loop. This means that mechanical stress and power dissipation in the sensing beams affect the electrical resistance change oppositely. In other words, an increase in the resistance of the sensing beams leads to a decrease in their power consumption, which consequently reduces their temperature. This correlation ultimately reduces the electrical resistance variations and thus the sensor gain.

The constant-current circuit is also modeled at the system level and presented in Fig. 5b. Considering a zero perturbation in the current that flows through the sensing beams, the transfer function from the input mechanical stress to the perturbation in the output voltage ( $T_{V\sigma}$ ) is obtained as follows:

$$T_{V\sigma} = \frac{R_0 I_0 \pi_0 K'}{1 - I_0^2 H_{T_0} F_{T_0}}. \quad (25)$$

In addition, the transfer function from the input stress to the change in the sensing beams' temperature in this circuit is:

$$T_{T\sigma} = \frac{R_0 \pi_0 K' I_0^2 F_{T_0}}{1 - I_0^2 H_{T_0} F_{T_0}}. \quad (26)$$

Using (25) and assuming the amplifier has a gain of  $A$ , the output of the constant-current circuit in Fig. 5b is found as:

$$V_{CCo} = A I_0 R_0 \frac{\pi_0 K'}{1 - I_0^2 H_{T_0} F_{T_0}} \sigma_{ip}. \quad (27)$$

Clearly, the output voltage is a linear function of normal stress, when temperature variations are factored in. In addition, the transfer functions reported in (25) and (26) are representative of a system with a positive feedback loop. Therefore, as opposed to the constant-voltage circuit, both mechanical stress and power-dissipation variation operate in the same manner to change the electrical resistance, leading to a higher sensor gain.

To conclude, when thermal variations are factored in, both circuits are expected to function linearly. However, the constant-current circuit is expected to have a larger gain. Note that these results are only valid for small variations in the beams' resistance and their temperature.

## VII. EXPERIMENTS

In order to compare the three readout circuits, the MEMS nanopositioner is actuated along the Y axis. The linear actuation mechanism is utilized to alleviate the quadratic nonlinearity of the electrostatic actuators [29]. To acquire reference results in time and frequency domains, displacement of the MEMS nanopositioner is directly measured using a Polytec MSA-100 laser vibrometer. During the experiments, the readout circuits are separately tested and the MSA and

the sensor outputs are simultaneously recorded and compared. The circuit parameters are initially adjusted to achieve a fair comparison, as described on the following.

### A. Test Conditions

To compare the sensor performance with Whetstone half-bridge and constant-voltage circuit, parameters of the circuits are adjusted such that their gains as well as the initial voltage on the sensing beams are equal. Considering Fig. 3a, the source voltage ( $V_c$ ) is tuned using (28) to equate the voltage on the sensing beams.

$$V_c = \frac{V_b R_0}{R + R_0}. \quad (28)$$

On the other hand, for equal gain condition, i.e.  $g_v = g_w$ , (10) and (13) are used. Employing this condition, the feedback resistor in the constant-voltage circuit (i.e.  $R_f$ ) is chosen as:

$$R_f = \frac{R R_0}{R + R_0}. \quad (29)$$

The same procedure, however, cannot be used for adjusting parameters of the constant-current circuit because the equal gain and voltage conditions cannot be simultaneously met. This is partially due to the fact that the constant-current circuit has a higher output gain, as discussed in Sec. VI. Therefore, we investigated two alternative possibilities.

In the first method, we assume that the initial electrical power dissipated in the piezoresistor is equal to that of the other two circuits. This is accomplished by adjusting the bias current to achieve an equal voltage on the sensing beams as the other readout circuits. Neglecting small changes during the operation, an equal power dissipation on the sensing beams is expected. In the second scenario, the gain of the constant-current circuit is equated to the gain of the other two readouts, i.e.  $g_c = g_v = g_w$ . To establish this condition, the initial voltage drop on the sensing beams is reduced to half of the equal-power condition.

### B. Parameter Adjustment and Circuit Realization

The initial electrical resistance of each sensing beam,  $R_0$ , is measured to be  $483 \Omega$ . We showed in [11], that the bias voltage in the Wheatstone half-bridge ( $V_b$ ), that leads to the finest sensor resolution is 6 V. The lumped resistors are selected as  $R = 496.6 \Omega$ , leading to a voltage of 3.1 V on the piezoresistors. The same voltage is adjusted for  $V_c$  in the constant-voltage circuit and the feedback resistors are adjusted to  $R_f = 245 \Omega$  according to (29).

The constant-current circuit is designed to feed a pair of DC bias currents with the same magnitude to the sensing beams. This current source provides a high output impedance to supply a low-noise DC current while eliminating the loading effect of the piezoresistors. Two op-amps are used on either side of the circuit to regulate the current passing through the PNP transistors. The op-amps maintain the DC voltage ( $V_{ref}$ ) across the resistors  $R_{set}$  which are placed between the voltage supply ( $V_c = 15 \text{ V}$ ) and the transistor emitter. In this configuration, the DC bias currents of  $I_c = 3.1 \text{ mA}$

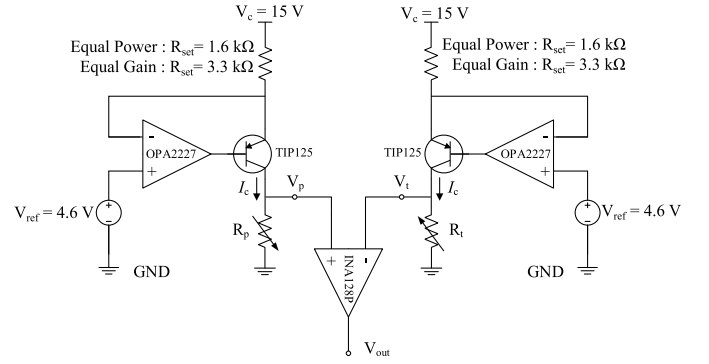


Fig. 6. A low-noise and high-output impedance current source circuit consisting of op-amps and PNP transistors.  $V_{ref}$  and  $R_{set}$  set the current delivered to pair of piezoresistors.

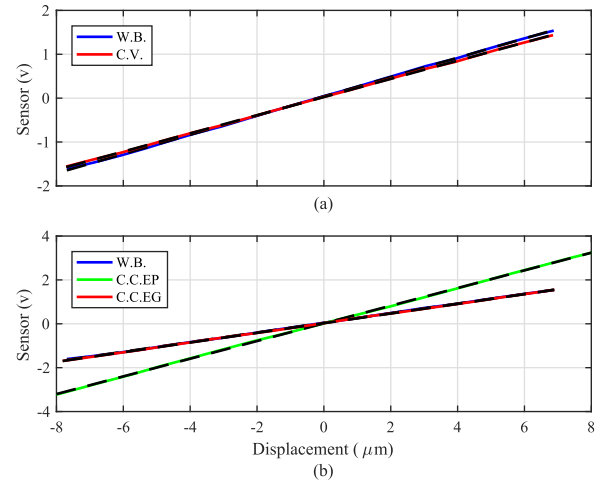


Fig. 7. Sensor output as a function of the input displacement with different readout circuits. In (a), the outputs for W.B. and C.V. are compared and (b) provides the comparison between the two different configurations of C.C.EG and C.C.EP circuits and W.B. The dotted lines represents the linear trend-lines.

are delivered to the pair of sensing beams by tuning  $R_{set} \approx 3.3 \text{ k}\Omega$  and  $V_{ref} = 4.6 \text{ V}$ . This current produces a voltage of approximately 1.5V on the sensing beams, biasing the sensor to function under the equal-gain condition. Technically, the constant resistors ( $R_{set}$ ) and the reference voltages ( $V_{ref}$ ) provide two degrees of freedom for setting the DC currents. However, the latter is used for fine tuning the current to eliminate any offset voltage at the output ( $V_{out}$ ) due to a potential mismatch between piezoresistor values. Note that to attain the equal-power test condition, the DC bias current is set to  $I_c = 6.5 \text{ mA}$  by tuning  $R_{set} \approx 1.6 \text{ k}\Omega$ .

## VIII. SENSOR CHARACTERIZATION

In this section, we report on the characterization of the bulk piezoresistive sensor in time and frequency domains using all readout circuits. For constant-current circuit, results are presented for both configurations of equal gain and equal power.

### A. Range and Linearity

In Fig. 7, the sensor output is shown as a function of shuttle beam displacement over a range of  $\pm 7.5 \mu\text{m}$ . The sensor

TABLE I  
THE CALIBRATION FACTOR, RESONANT FREQUENCY, MAPPING ERROR,  $1\sigma$ -RESOLUTION, AND DYNAMIC RANGE OF THE SENSOR OUTPUT OBTAINED EXPERIMENTALLY FOR DIFFERENT READOUT CIRCUITS

Readout Circuit	W.B.	C.V.	C.C.EG.	C.C.EP.
Calibration Factor ( $V/\mu m$ )	0.219	0.207	0.220	0.403
Resonant Frequency (Hz)	3450	3449	3645	3575
Mapping Error (%)	1.18	0.47	0.46	0.48
$1\sigma$ -Resolution (nm)	1.6	1.9	3.7	4.2
DNR (dB)	79.44	77.95	72.16	71.62

shows a linear behavior with all readout circuits. The slope of the trend line, which is considered as the calibration factor of the sensor, is shown in Table I. By equating gains of all circuits, we find that all calibration factors are nearly identical with the exception of the constant-current circuit biased in equal-power modality. For this configuration, the sensor shows a much higher gain (about 1.8 times larger) as is also predicted by the system-theoretic model in Sec. VI.

To investigate the linearity of the sensor, the mapping error ( $M$ ) is defined as follows:

$$M = \pm \frac{e_{\max}}{FSR} \times 100 \quad (30)$$

where  $e_{\max}$  is the maximum deviation of experimental points from the fitted line, and FSR is the full-scale range of the sensor output. For all circuits,  $M$  is obtained and reported in Table I. Considering this error, constant-voltage and -current circuits show an almost equally linear performance. They both have a superior linearity compared to Wheatstone half-bridge. Implementation of this readout, however, leads to an increase in  $M$  by a factor of about 2.5, indicating its significantly larger nonlinearity.

### B. Frequency Domain Behavior

Frequency domain experiments are performed by applying a wide-band chirp signal to the electrostatic actuators. The displacement of the shuttle structure is then directly measured using the MSA. The frequency response of the sensor for different readout circuits is obtained using a FRF analyzer (ONO SOKKI CF-9400).

The frequency response obtained from the sensor is compared with the MSA results in Fig. 8. We observe that the sensor is able to capture the dynamics of the nanopositioner over a bandwidth of 20 kHz with all readout circuits.

In Table I, the resonant frequencies of the MEMS nanopositioner are also reported. Although driving the sensor using the constant-voltage and Wheatstone half-bridge results in nearly identical resonant frequencies, the use of the constant-current configurations results in slightly larger resonances; about 5.6% and 3.6% larger for equal-gain and equal-power configurations, respectively. This deviation is also observed in the MSA data and is believed to be originated from the difference in the thermally-induced axial forces along the sensing beams. Since these beams simultaneously function as a part of the flexural mechanism, the softening effect originated

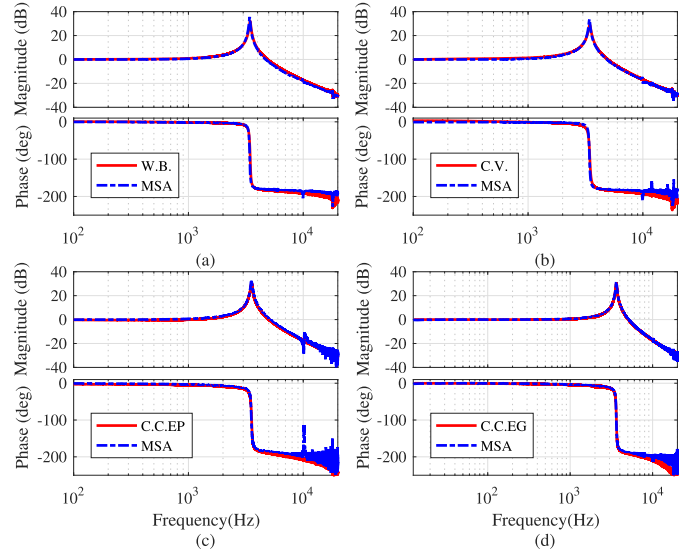


Fig. 8. Frequency responses obtained from the MSA, i.e. the actual displacement, and the displacement sensor with different readout circuits.

from this thermal stress can ultimately reduce the resonant frequency of the MEMS nanopositioner [11]. By using the constant-current circuit with equal-gain configuration both voltage and current of the sensing beams are at their lowest, and therefore, the beams experience a lower temperature and consequently a lower thermal axial stress, leading to the largest resonant frequency.

We have adjusted the initial current along the sensing beams to achieve the same power dissipation in equal-power constant-current circuit compared to C.V. and W.B. readouts. However, a slight deviation is observed in the voltage of the beams during the sensor operation, which is most likely due to the slow changes in the resistance of the doped silicon due to temperature elevation. Comparing the resonant frequencies in Table I, we may conclude that the thermal axial stress and consequently the equilibrium temperature of the beams in equal-power constant-current circuit are slightly lower compared to other two readouts.

### C. Noise and Resolution

We investigate noise performance of the sensor with all readout circuits in both time and frequency domains. The tests are performed on an optical table, with the actuators electrically grounded and the device and the associated circuitry placed in an isolation metal box to eliminate electrical and mechanical disturbances. Using each circuit, the sensor output is recorded at the sampling rate of 115 kHz, while a low-pass filter (SR650 Stanford Research) with cut-off frequency of 15 kHz and 115 dB/octave roll-off is placed in the path. We use the time domain data to determine the root-mean-square (RMS) value of the output signal. The calibration factors in Table I are then used to convert the noise RMS to displacement resolution. The  $1\sigma$ -resolution of the sensor is reported in Table I. The results indicate that the resolution of the sensor with Wheatstone half-bridge and constant-voltage

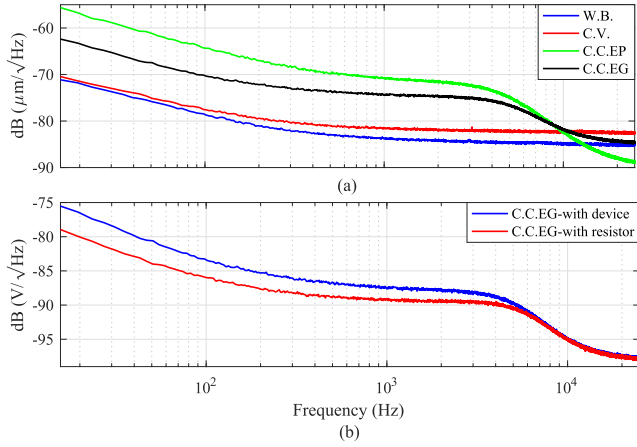


Fig. 9. (a) The power spectral density of noise with different readout circuits. The sensor with the constant-current circuit in both equal-gain (C.C.EG.) and equal power (C.C.EP) configurations shows the largest noise level. (b) Power spectral density of noise at the constant-current circuit output biased in the equal-gain condition for the sensor and when the sensing beams are replaced with comparable lumped resistors.

circuit are almost equal. However, the constant-current circuit increases the noise level, deteriorating the resolution by more than a factor of two.

To further investigate performance of the bulk piezoresistive sensor with different readout circuits, we obtain the dynamic range of the sensor. As described in [13], the dynamic range (DNR) is defined as

$$\text{DNR} = 20 \log \left( \frac{\text{FSR}}{\text{resolution}} \right) \quad (31)$$

where FSR is the full scale range of the device. With the Wheatstone bridge, constant-voltage and constant-current circuit in equal-gain configuration, the maximum displacement range is approximately  $15 \mu\text{m}$ . With the constant-current circuit in equal-power condition, the range increases to approximately  $16 \mu\text{m}$ . From Table. I, we observe that the DNR decreases with constant-current circuit since the sensor output noise increases. However, the achievable displacement range is comparable to other readout circuits.

Fig. 9a shows the power spectral density (PSD) for the sensor noise with various readout circuits. For a better comparison, the PSD is converted to displacement using the sensor's calibration factors for each readout circuits. The sensor displays a significant  $1/f$ -noise, which is inherent to piezoresistive phenomenon [12], [30], [31]. The noise performances of Wheatstone half-bridge and constant-voltage readouts are nearly identical. A slightly higher noise level in the constant-voltage circuit can be attributed to the extra active components in this circuit. The thermal noise floor is observed after a corner frequency of about 800 Hz.

A higher power in the noise signal with constant-current configuration can also be observed in the frequency domain. The PSD of noise also shows a roll-off at about 5 kHz. The same response is observed when the sensing beams are replaced with comparable lumped resistors; see Fig. 9b, indicating that the roll-off behavior originates from the current-source circuit. This property of the circuit also adds a slight phase lag to the sensor response. In comparison with the

other two readouts, the sensor response with constant-current circuit in both biasing conditions has about  $20^\circ$  more phase drop at 10 kHz.

In the system-theoretic model presented in Sec. VI, the thermal and  $1/f$  noise can be included as the resistance fluctuations of the piezoresistors [27], [32]. Therefore, the signal to noise ratio (SNR) at the output should be independent of the circuit gain. Despite this, the constant-current circuit shows a higher noise level, and consequently a lower SNR, compared to the constant-voltage circuit. This can be attributed to the noise generated by the active components of the circuit. Shown in Fig. 9b, by replacing the piezoresistors with the lumped resistors, the spectrum of the noise only drops by 5 dB across the bandwidth, indicating that the circuit's active components, i.e. the op-amps and PNP transistors, are the main sources of noise. Switching from the equal-gain to equal-power condition, on the other hand, leads to an increase of 6 dB in the noise power spectral density of the constant-current circuit shown in Fig. 9a. This is most likely due to a higher working temperature of the sensing beams at the equal-power condition. In addition, a larger bias current here leads to a larger level of the shot noise at the BJT transistors.<sup>1</sup>

We performed simulations to analyze the effect of output-referred noise in the readout circuits when the piezoresistive sensors are replaced with comparable resistors. As expected, a higher level of noise was obtained in the output of the constant-current circuit due to the shot noise.

Although the noise level of the constant-current circuit is obtained to be larger than the other two readouts, the resolution that we achieved in this work with the custom-designed current-source circuit shows a five-fold improvement compared with the resolution that is obtained in [35] using a commercially-available current-source IC. This is in spite of the fact that the bandwidth for the noise measurement in [35] was also limited to about 1 kHz, as opposed to the achieved bandwidth of 15 kHz in this study.

## IX. CONCLUSION

Characteristics of a MEMS bulk piezoresistive displacement sensor with three different readout circuits are explored. Analytical as well as system-theoretic models are proposed to study the sensor behavior. The sensor characterization reveals a linear behavior within a range of  $\pm 7.5 \mu\text{m}$  with all readouts. Using the constant-voltage and constant-current circuits leads to a superior linearity. Predicted also by the system-theoretic model, the constant-current circuit shows a larger sensitivity, about 1.9 times, than the other two circuits at the same bias. The larger sensitivity encouraged us to consider equal gain and equal power test modalities for this circuit to achieve a fair comparative study. The sensor shows the best resolution of 1.6 nm with the Wheatstone half-bridge circuit. The resolution degrades to the coarsest value of 4.2 nm for the constant-current circuit biased at equal power modality. In the

<sup>1</sup>The shot noise in BJTs is proportional to the root square of the collector current [33], [34]. Therefore, increasing the bias current in constant-current circuit from 3.1 mA in equal-gain to 6.5 mA in equal-power condition leads to an increase of about 3 dB in the level of the shot noise.



frequency domain, the dynamics of the MEMS nanopositioner is captured by the sensor within the bandwidth of 20 kHz with all circuits. We conclude that driving the sensor with a constant voltage leads to a better compromise in terms of the linearity, bandwidth, and noise as well as a more straightforward circuit implementation.

#### APPENDIX

For each sensing beam, we may write the Ohm's law as:

$$E = \rho J \quad (32)$$

where  $\rho$  is the resistivity of the doped silicon, and  $E$  and  $J$  are the electric field and current density along the beam, respectively. Almost the entire electric current flows through the doped cross section of the beam due to its low resistance. Therefore, the induced resistance change in the beams is mainly attributed to the piezoresistivity of the doped silicon. We may write the following for resistivity of the beams in compression ( $\rho_p$ )

$$\rho_p = \rho_0 [1 + \sigma_p |\pi_l(z)|] \quad (33)$$

and in tension ( $\rho_t$ )

$$\rho_t = \rho_0 [1 - \sigma_t |\pi_l(z)|]. \quad (34)$$

In (33) and (34),  $\pi_l(z)$  denotes the piezoresistivity coefficient of the doped silicon and  $\rho_0$  is the initial resistivity of the silicon in the absence of mechanical stress. The coordinate  $z$  is defined on the cross section and along the thickness of the beam, as shown in the close-up view in Fig. 1. Piezoresistivity of silicon is a strong function of the dopant type and its concentration as well as the temperature [36]. Since dopant concentration is non-uniform across the cross section,  $\pi_l(z)$  is a function of depth ( $z$ ), i.e.:

$$\pi_l(z) = \pi_0 f(z). \quad (35)$$

Due to the unknown concentration profile of dopants,  $f(z)$  in (35) can not be determined, however as shown later, this does not limit our comparative study. Knowing the electric field obtained in (32), voltage difference across the sensing beams is found to be:

$$V_{t,p} = \int_0^l E_{t,p} dx, \quad (36)$$

where  $E_t$  and  $E_p$  are the electric fields along the beams in tensile and compression, respectively. Here,  $l$  denotes the length of the sensing beams. In Fig. 1, the ultimate depth where the dopant concentration becomes negligible is designated by  $d$ . Since a negligible current passes through the undoped cross section, the current along the sensing beams with the width (in-plane dimension) of  $w$  is:

$$I_{t,p} = \int J_{t,p} dA = \int_d^{t_s/2} w J_{t,p} dz \quad (37)$$

Due to the symmetry, only the longitudinal electric current along the beams needs to be considered. This is equivalent to

having a constant electric field along the beams, leading to  $V_t = E_t l$  and  $V_p = E_p l$ . Thus  $I_t$  can be obtained as:

$$I_t = \int_d^{t_s/2} w \frac{V_t}{\rho_t l} dz. \quad (38)$$

Substituting  $\rho_t$  from (34) in (38), we have:

$$I_t = \frac{w V_t}{l} \int_d^{t_s/2} \frac{dz}{\rho_0 [1 - \sigma_t \pi_0 f(z)]}. \quad (39)$$

We assume that  $\sigma_t \pi_0 f(z) \ll 1$ . This is justified since  $\pi_0$  is orders of magnitude smaller than the stress level ( $\sigma_t \times f(z)$ ) [23]. Hence, (39) can be approximated as:

$$\begin{aligned} I_t &\cong \frac{w V_t}{l \rho_0} \int_d^{t_s/2} [1 + \sigma_t \pi_0 f(z)] dz \\ &= \frac{w V_t}{l \rho_0} [(t_s/2 - d) + \sigma_t \pi_0 K] \end{aligned} \quad (40)$$

where:

$$K = \int_d^{t_s/2} f(z) dz. \quad (41)$$

Similarly for the current along the sensing beam under compression, i.e.  $I_p$ , we have:

$$I_p = \frac{w V_t}{l \rho_0} [(t_s/2 - d) - \sigma_p \pi_0 K]. \quad (42)$$

These expressions for  $I_t$  and  $I_p$  show that the electric current consists of two components, one due to the bias voltage and the other due to the induced mechanical stress. Resistance of a beam under tensile load (i.e.  $R_t$ ) can be obtained using the Ohm's law:

$$R_t = \frac{l \rho_0}{w [(t_s/2 - d) + \sigma_t \pi_0 K]} \cong R_0 [1 + \sigma_t \pi_0 K']. \quad (43)$$

where

$$R_0 = \frac{l \rho_0}{W (t_s/2 - d)} \quad (44a)$$

$$K' = \frac{K}{(t_s/2 - d)}. \quad (44b)$$

Here,  $R_0$  is the initial resistance of the beam. Finally, for the beam under compression we have:

$$R_p = \frac{l \rho_0}{w [(t_s/2 - d) - \sigma_p \pi_0 K]} \cong R_0 (1 + \sigma_p \pi_0 K'). \quad (45)$$

Note that the doping profile,  $f(z)$ , in (41) is required to calculate the exact values of  $R_p$  and  $R_t$ . However, this is not necessary for this comparative study.

#### ACKNOWLEDGMENT AND DISCLAIMER

*Acknowledgment:* "This material is based upon work supported by the U.S. Department of Energy's Office of Energy Efficiency and Renewable Energy (EERE) under the Advanced Manufacturing Office Award Number DE-EE0008322."

*Disclaimer:* "This report was prepared as an account of work sponsored by an agency of the United States Government. Neither the United States Government nor any agency thereof, nor any of their employees, makes any

warranty, express or implied, or assumes any legal liability or responsibility for the accuracy, completeness, or usefulness of any information, apparatus, product, or process disclosed, or represents that its use would not infringe privately owned rights. Reference herein to any specific commercial product, process, or service by trade name, trademark, manufacturer, or otherwise does not necessarily constitute or imply its endorsement, recommendation, or favoring by the United States Government or any agency thereof. The views and opinions of authors expressed herein do not necessarily state or reflect those of the United States Government or any agency thereof."

## REFERENCES

- [1] D. K. Shaeffer, "MEMS inertial sensors: A tutorial overview," *IEEE Commun. Mag.*, vol. 51, no. 4, pp. 100–109, Apr. 2013.
- [2] B. Krijnen *et al.*, "A single-mask thermal displacement sensor in MEMS," *J. Micromech. Microeng.*, vol. 21, no. 7, 2011, Art. no. 074007.
- [3] M. Maroufi, A. G. Fowler, A. Bazaei, and S. O. R. Moheimani, "High-stroke silicon-on-insulator MEMS nanopositioner: Control design for non-raster scan atomic force microscopy," *Rev. Sci. Instrum.*, vol. 86, Jan. 2015, Art. no. 023705.
- [4] M. G. Ruppert, S. I. Moore, M. Zawierda, A. J. Fleming, G. Putrino, and Y. K. Yong, "Multimodal atomic force microscopy with optimized higher eigenmode sensitivity using on-chip piezoelectric actuation and sensing," *Nanotechnology*, vol. 30, no. 8, 2019, Art. no. 085503.
- [5] I. W. Rangelow *et al.*, "Review Article: Active scanning probes: A versatile toolkit for fast imaging and emerging nanofabrication," *J. Vac. Sci. Technol. B, Microelectron.*, vol. 35, no. 6, Nov. 2017, Art. no. 06G101.
- [6] Y.-S. Choi, Y. Zhang, and D.-W. Lee, "A thermal-driven silicon micro XY-stage integrated with piezoresistive sensors for nano-positioning," *J. Micromech. Microeng.*, vol. 22, no. 5, 2012, Art. no. 055002.
- [7] A. J. Fleming, "A review of nanometer resolution position sensors: Operation and performance," *Sens. Actuators A, Phys.*, vol. 190, pp. 106–126, Feb. 2013.
- [8] M. Maroufi, A. G. Fowler, and S. O. R. Moheimani, "MEMS for nanopositioning: Design and applications," *J. Microelectromech. Syst.*, vol. 26, no. 3, pp. 469–500, Jun. 2017.
- [9] M. Maroufi and S. O. R. Moheimani, "Characterization of piezoresistive and electrothermal sensors in MEMS devices," in *Proc. IEEE SENSORS Conf.*, Orlando, FL, USA, Oct./Nov. 2016, pp. 1–3.
- [10] A. Bazaei, M. Maroufi, A. Mohammadi, and S. O. R. Moheimani, "Displacement sensing with silicon flexures in MEMS nanopositioners," *J. Microelectromech. Syst.*, vol. 23, no. 3, pp. 502–504, Jun. 2014.
- [11] M. Maroufi, A. Bazaei, A. Mohammadi, and S. O. R. Moheimani, "Tilted beam piezoresistive displacement sensor: Design, modeling, and characterization," *J. Microelectromech. Syst.*, vol. 24, no. 5, pp. 1594–1605, Oct. 2015.
- [12] M. Maroufi and S. O. R. Moheimani, "A 2DOF SOI-MEMS nanopositioner with tilted flexure bulk piezoresistive displacement sensors," *IEEE Sensors J.*, vol. 16, no. 7, pp. 1908–1917, Apr. 2016.
- [13] M. Maroufi, H. Alemansour, M. B. Coskun, and S. O. R. Moheimani, "An adjustable-stiffness MEMS force sensor: Design, characterization, and control," *Mechatronics*, vol. 56, pp. 198–210, Dec. 2018.
- [14] M. Dukic, J. D. Adams, and G. E. Fantner, "Piezoresistive AFM cantilevers surpassing standard optical beam deflection in low noise topography imaging," *Sci. Rep.*, vol. 5, Nov. 2015, Art. no. 16393.
- [15] M. Santosh, K. C. Behera, and S. C. Bose, "Design of an on chip read-out circuit for piezo-resistive MEMS pressure sensor," in *Proc. Int. Conf. Devices, Circuits Syst. (ICDCS)*, Mar. 2012, pp. 94–98.
- [16] S. Kon, K. Oldham, and R. Horowitz, "Piezoresistive and piezoelectric MEMS strain sensors for vibration detection," *Proc. SPIE*, vol. 6529, Apr. 2007, Art. no. 65292V.
- [17] G. E. Fantner, D. J. Burns, A. M. Belcher, I. W. Rangelow, and K. Youcef-Toumi, "DMCMN: In depth characterization and control of AFM cantilevers with integrated sensing and actuation," *J. Dyn. Syst., Meas., Control*, vol. 131, no. 6, Nov. 2009, Art. no. 061104.
- [18] X. Liu *et al.*, "A novel scanning force microscopy probe with thermal-electrical actuation and piezo-resistive sensing," *J. Micromech. Microeng.*, vol. 28, no. 11, 2018, Art. no. 115003.
- [19] A. Thanachayanont and S. Sangtong, "Low-voltage current-sensing CMOS interface circuit for piezo-resistive pressure sensor," *ETRI J.*, vol. 29, no. 1, pp. 70–78, Feb. 2007.
- [20] S. J. Azhari and H. Kaabi, "AZKA cell, the current-mode alternative of Wheatstone bridge," *IEEE Trans. Circuits Syst. I, Fundam. Theory Appl.*, vol. 47, no. 9, pp. 1277–1284, Sep. 2000.
- [21] S. Nag, N. S. Kale, V. R. Rao, and D. K. Sharma, "An ultra-sensitive  $\Delta R/R$  measurement system for biochemical sensors using piezoresistive micro-cantilevers," in *Proc. Annu. Int. Conf. IEEE Eng. Med. Biol. Soc.*, Sep. 2009, pp. 3794–3797.
- [22] N. A. Gilda, S. Nag, S. Patil, M. S. Baghini, D. K. Sharma, and V. R. Rao, "Current excitation method for  $\Delta R$  measurement in piezo-resistive sensors with a 0.3-ppm resolution," *IEEE Trans. Instrum. Meas.*, vol. 61, no. 3, pp. 767–774, Mar. 2012.
- [23] M. Maroufi and S. O. R. Moheimani, "An SOI-MEMS piezoelectric torsional stage with bulk piezoresistive sensors," *IEEE Sensors J.*, vol. 17, no. 10, pp. 3030–3040, May 2017.
- [24] A. Mohammadi, A. G. Fowler, Y. K. Yong, and S. O. R. Moheimani, "A feedback controlled MEMS nanopositioner for on-chip high-speed AFM," *J. Microelectromech. Syst.*, vol. 23, no. 3, pp. 610–619, 2014.
- [25] A. Cowen, G. Hames, D. Monk, S. Wilcenski, and B. Hardy, "SOIMUMPs design handbook, revision 8.0," MEMSCAP Inc., Durham, NC, USA, 2011.
- [26] A. Sebastian and D. Wiesmann, "Modeling and experimental identification of silicon microheater dynamics: A systems approach," *J. Microelectromech. Syst.*, vol. 17, no. 4, pp. 911–920, Aug. 2008.
- [27] A. Mohammadi, S. O. R. Moheimani, and M. R. Yuce, "A comparison of two excitation modes for MEMS electrothermal displacement sensors," *IEEE Electron Device Lett.*, vol. 35, no. 5, pp. 584–586, May 2014.
- [28] M. Cauchi, I. Grech, B. Mallia, P. Mollicone, and N. Sammut, "The effects of cold arm width and metal deposition on the performance of a U-beam electrothermal MEMS microgripper for biomedical applications," *Micromachines*, vol. 10, no. 3, p. 167, 2019.
- [29] M. Maroufi, A. Bazaei, and S. O. R. Moheimani, "A high-bandwidth MEMS nanopositioner for on-chip AFM: Design, characterization, and control," *IEEE Trans. Control Syst. Technol.*, vol. 23, no. 2, pp. 504–512, Mar. 2014.
- [30] J. C. Doll and B. L. Pruitt, *Piezoresistor Design and Applications* (Microsystems and Nanosystems). New York, NY, USA: Springer, 2013.
- [31] A. A. Barlian, W.-T. Park, J. R. Mallon, Jr., A. J. Rastegar, and B. L. Pruitt, "Review: Semiconductor piezoresistance for microsystems," *Proc. IEEE*, vol. 97, no. 3, pp. 513–552, Mar. 2009.
- [32] P. H. Handel, "Quantum approach to  $\frac{1}{f}$  noise," *Phys. Rev. A, Gen. Phys.*, vol. 22, pp. 745–757, Aug. 1980.
- [33] A. Van der Ziel, *Noise in Solid State Devices and Circuits*. Hoboken, NJ, USA: Wiley, 1986.
- [34] Motorola, *Small-Signal Transistors, FETs, and Diodes Device Data*. Motorola Semicond. Products, Phoenix, AZ, USA, 2000.
- [35] N. Nikoienjad, M. Maroufi, and S. O. R. Moheimani, "Characterization of a tilted-beam piezoresistive MEMS sensor with current-drive readout circuit," in *Proc. Amer. Control Conf. (ACC)*, Jul. 2019, pp. 2483–2488.
- [36] Y. Kanda and Y. Kanda, "A graphical representation of the piezoresistance coefficients in silicon," *IEEE Trans. Electron Devices*, vol. 29, no. 1, pp. 64–70, Jan. 1982.



**Mohammad Maroufi** received the double B.Sc. degrees in mechanical engineering and applied physics and the master's degree in mechatronics from the Amirkabir University of Technology (Tehran Polytechnic), in 2008 and 2011, respectively, and the Ph.D. degree in electrical engineering from the University of Newcastle, Callaghan, NSW, Australia, in 2015. From 2015 to 2019, he continued his career by holding Research Associate and then Research Scientist postdoctoral position at the University of Texas at Dallas, Richardson, TX, USA. He has authored over 50 peer-reviewed articles. His research interests include the development of ultrahigh-precision mechatronic systems, design and control of MEMS nanopositioners, microsensors design, and video-rate scanning probe microscopes.



**Nastaran Nikooinnejad** received the B.Sc. degree in electrical engineering from Shiraz University in 2006 and the M.Sc. degree in electrical engineering from Amirkabir University of Technology in 2009. She is currently pursuing the Ph.D. degree with the Department of Electrical and Computer Engineering, University of Texas at Dallas. Her research interests include high-precision control of MEMS devices, video-rate atomic force microscopy, and signal and image processing.



**Mohammad Mahdavi** received the B.Sc. and M.Sc. degrees in electrical engineering from The University of Tehran, Tehran, Iran, in 2007 and 2010, respectively, and the Ph.D. degree in electrical engineering from The University of Texas at Dallas in May 2018. He is currently a Research Associate with the Department of Systems Engineering, The University of Texas at Dallas. His main research interests involve design, microfabrication and characterization of microelectromechanical systems (MEMS), with especial focus on piezoelectric

microcantilevers and resonant piezoelectric devices/sensors.



**S. O. Reza Moheimani** (F'11) currently holds the James Von Ehr Distinguished Chair in science and technology with the Department of Systems Engineering, The University of Texas at Dallas, with appointments in Electrical and Computer Engineering and Mechanical Engineering Departments. His current research interests include applications of control and estimation in high-precision mechatronic systems, high-speed scanning probe microscopy, and atomically precise manufacturing of solid-state quantum devices. He is a fellow of the IFAC and the Institute of Physics, U.K. He is a recipient of several awards, including the IFAC Nathaniel B. Nichols Medal and the IEEE Control Systems Technology Award. He is the Editor-in-Chief of *Mechatronics*.